Experimental Aeroelastic Characterization of a Very Flexible Wing in Steady and Unsteady Inflow

Mertens, C.; Sodja, J.; Sciacchitano, A.; van Oudheusden, B.W.

DOI
10.2514/6.2022-1344

Publication date
2022

Document Version
Final published version

Published in
AIAA SCITECH 2022 Forum

Citation (APA)
Mertens, C., Sodja, J., Sciacchitano, A., & van Oudheusden, B. W. (2022). Experimental Aeroelastic Characterization of a Very Flexible Wing in Steady and Unsteady Inflow. In *AIAA SCITECH 2022 Forum* Article AIAA 2022-1344 (AIAA Science and Technology Forum and Exposition, AIAA SciTech Forum 2022). https://doi.org/10.2514/6.2022-1344

AIAA SciTech Forum
January 3-7, 2022, San Diego, CA & Virtual
AIAA SCITECH 2022 Forum

10.2514/6.2022-1344

Experimental Aeroelastic Characterization of a Very Flexible Wing in Steady and Unsteady Inflow

Christoph Mertens[1], Jurij Sodja[2], Andrea Sciacchitano[3] and Bas W. van Oudheusden[4]
Faculty of Aerospace Engineering, Delft University of Technology, 2629HS Delft, The Netherlands

The aeroelastic response of a very flexible wing in steady and unsteady inflow conditions is measured in a wind tunnel experiment. An integrated aeroelastic characterization is performed with a non-intrusive optical setup that allows simultaneous measurements of the structural motion and the flow field around the wing. The experimental aerodynamic loads that are inferred from the flow field measurements are in very good agreement with reference data from a force balance. Prior to the wind tunnel experiment, results of the numerical modal analysis of a structural model of the wing are compared with the experimental results from a ground vibration test. An aeroelastic model validation is achieved by applying the experimental aerodynamic loads to the structural model of the wing. The results of this structural analysis are compared with the measured structural response in the wind tunnel for steady inflow conditions, yielding differences of around 15% in tip displacements when using a linear structural model.

I. Nomenclature

c = chord length, m
C_l = section lift coefficient
C_L = wing lift coefficient
d = deflection, m
f_{FEM} = modal frequency in finite-element model, Hz
f_{GVT} = modal frequency in ground vibration test, Hz
f_g = frequency of the gust, Hz
k = reduced frequency
L' = Lift per unit span, N/m
s = span width, m
t = time, s
T = period, s
u = streamwise velocity, m/s
U_∞ = freestream velocity, m/s
α = geometric angle of attack, deg
β = gust vane angle, deg
β_g = gust vane motion amplitude, deg
Γ = circulation, $\mathrm{m^2/s}$
ε = twist angle, deg
ρ = air density, $\mathrm{kg/m^3}$
σ = standard deviation

II. Introduction

A current trend in aviation is towards the use of more flexible lifting structures, mainly driven by the desire to improve efficiency through saving structural weight. As a consequence, larger structural deformations are observed and aeroelastic effects become more relevant. For very flexible wings, the structural deformation can become so large as to produce nonlinear aerodynamic and structural effects that violate the assumptions employed by linear aeroelastic prediction models [1]. While the development of novel improved aeroelastic prediction methods that account for these nonlinear effects is currently ongoing [2-4], an experimental benchmark of a highly flexible wing, known as the Pazy wing, has recently been introduced to support these activities with experimental reference data [5]. This wing has been shown to sustain very large deformations, with wingtip displacements of up to 50% of the span.

---

[1] PhD Candidate, Aerodynamics department, AIAA student member, corresponding author: C.Mertens@tudelft.nl
[2] Senior Researcher, Aerospace structures and materials department, AIAA member
[3] Assistant Professor, Aerodynamics department
[4] Associate Professor, Aerodynamics department

The production of reference data from aeroelastic wind tunnel experiments is challenging due to the interaction of the three forces comprising the Collar's triangle (aerodynamic, inertial, elastic) [6], which would ideally all be quantified based on the experimental measurement data. A variety of sensors exists to measure individual physical quantities that allow the determination of each of the forces locally (e.g., pressure transducers, accelerometers, strain gauges) or in a global sense at the wing root with load cells or a force balance, but their coordinated use results in complex and expensive experimental setups. Additionally, installed sensors are invasive to the experimental model, thus modifying its mass and stiffness distributions, and typically achieve only a relatively low spatial resolution due to space limitations inside the model. As a result, the experimental reference data from aeroelastic wind tunnel measurements on flexible wings that is available in the published literature is usually limited to only a few parameters, such as the wingtip deflection or the frequency of the dynamic motion [7].

Optical measurement techniques, such as photogrammetry [8] for measuring the structural response and particle image or tracking velocimetry (PIV/PTV, [9]) for aerodynamic measurements, permit non-intrusive field measurements and hence overcome many of the limitations associated with the use of installed sensors. On the other hand, the drawback of these non-intrusive techniques is that the determination of the aeroelastic forces from the measured quantities, such as structural displacements or flow velocity, is not straightforward. This topic has therefore been subject to considerable research efforts in recent years [10-12]. Despite this complication, the advantages of optical measurement techniques are prevailing and several recent studies have employed optical measurement techniques for characterizing fluid-structure interactions in wind tunnel experiments [13-15]. A common thread in these studies is tackling the complication of the experimental setup and/or the data processing that arises from the coordinated use of different optical measurement systems or techniques to obtain the structural and the flow measurements. A measurement approach that does not suffer from this limitation is Lagrangian Particle Tracking (LPT). It was recently shown that LPT, implemented via the Shake-The-Box algorithm [16], can form the basis for a single system capable of providing an integrated measurement of the structural displacements and aerodynamic loads on unsteady airfoils on a relatively large scale (wing span on the order of 1 m) [17]. The structural response is hereby determined by tracking fiducial markers on the experimental model, while the aerodynamic loads are inferred from flow field measurements, where helium-filled soap bubbles (HFSB) are used as flow tracers [18]. In a recent demonstration study, this approach has been successfully used to determine the three forces in Collar's triangle acting on a flexible wing subjected to steady and unsteady inflow conditions [19].

In the current study, LPT measurements are used to characterize the aeroelastic response of a highly flexible wing in steady and unsteady inflow conditions. The design of the wing is very similar to the benchmark wing that was introduced in [5]. In this particular investigation, wingtip displacements of nearly 25% of the span are observed. This study aims to extend the current state of the art in aeroelastic measurement technology by providing complete flow field measurements around the wing along the entire span, as well as structural deformation measurements, in various aeroelastic conditions, by presenting results from steady and unsteady inflow conditions. Furthermore, a finite-element method (FEM) structural model of the wing is first validated with an experimental ground vibration test (GVT) and subsequently used to perform an aeroelastic model validation based on the wind tunnel measurement data. This validation consists of determining the aerodynamic loads from the flow field measurements and calculating the structural response to these loads with the FEM model, which is then compared to the structural measurements of the wing deformation to assess the performance of the structural model.

III. Experimental procedures

A. Delft-Pazy Wing Model

The experimental model in this study is nearly identical to the benchmark Pazy wing that is described in detail in [5]. The wing has a reference span of $s = 550$ mm, a chord length of $c = 100$ mm and a NACA 0018 airfoil section with a 300 mm long wing tip rod. The wing structure consists of an aluminum spar and a 3D printed nylon chassis. The assembly of the Delft-Pazy wing is performed analogous to the procedure described in [5]. The main difference to the benchmark Pazy wing design is the reduced thickness of the aluminum plate representing the spar of the Delft-Pazy wing, which is 1.5 mm, as opposed to 2.25 mm for the original benchmark wing. The purpose of this design modification is to achieve similarly large deformations as observed in [5] at the lower wind tunnel speed, which was adjusted downwards to facilitate the LPT measurements of the wing with the optical setup present in the wind tunnel test section (see Section III.C). The skin of the Delft-Pazy wing is made of Oralight black foil. A grid of white circular markers with a diameter of 1.5 mm is painted on the wing surface at the spanwise locations of the ribs and on the wingtip rod to perform the non-intrusive measurements of the structural response of the wing in the wind tunnel. The wing geometry and the fiducial marker grid specifications are shown in Figure 1.

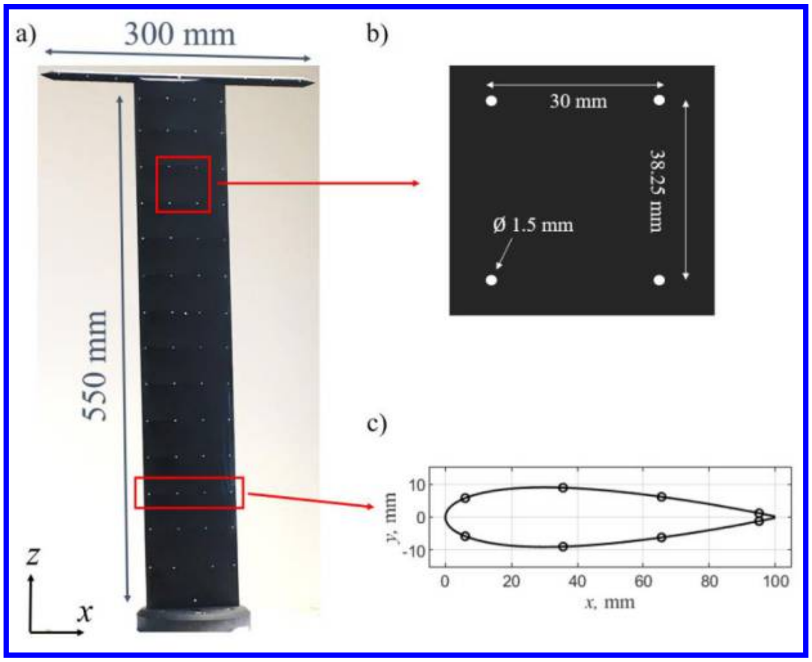

Figure 1: Delft-Pazy wing with fiducial marker grid, a) photo of the wing, b) dimensions of the marker grid, c) distribution of markers along the chord

It should be noted that the density of the marker pattern is insufficient to directly measure the wing deformation in terms of the local strain. Instead, the purpose of the structural marker measurements is twofold; firstly, the marker measurements are used to transform the measurement coordinate system into wind tunnel coordinates as described in Section III.D, and secondly, they are used to determine the deformed wing shape with the procedure described in Section IV.B, which is in turn used for the validation of the structural response that is calculated with the FEM model. Additionally, the marker-based wing shape is used during the aerodynamic load determination based on the flow field measurements in Section V.

B. Ground Vibration Tests

Two GVTs were conducted on the Delft-Pazy wing model. The first GVT was performed before the application of the skin to the chassis and the second GVT was performed afterwards. The motivation for this procedure is to investigate the effect of the skin on the stiffness characteristics of the wing, since the structural modeling of the skin was found to be challenging in [5]. The GVT measurements were conducted with a Polytec PSV-500 laser scanning vibrometer in the frequency range up to 800 Hz and postprocessed with SimCenter TestLab. An overview of the experimental setup of the GVT is shown in Figure 2a. Vibration data was acquired at 37 different measurement points on the wing (see Figure 2b), and the data from 10 measurements was averaged for each measurement point. The excitation of the wing model was achieved with a Maul-Theet vlmpact-61 automatic modal hammer. The impact point of the modal hammer was near the leading edge of the wing at around one quarter of the wingspan measured from the base, between the third and the fourth rib. The GVT results are correlated in this study with a FEM model of the wing using the correlation tool in SimCenter 3D. The FEM model of the Delft-Pazy wing was derived from the FEM model of the original Pazy wing by adjusting the spar thickness to match the reduced spar plate thickness.

C. Wind Tunnel Setup

Wind tunnel experiments were conducted in the Open Jet Facility (OJF) at Delft University of Technology. The OJF is an open test section, closed-loop wind tunnel with an octagonal outlet that spans $2.85\ \mathrm{m} \times 2.85\ \mathrm{m}$, which was operated at a freestream velocity of $U_\infty = 18\ \mathrm{m/s}$ during the experiments, corresponding to a Reynolds number of $\mathrm{Re} = 120\,000$ based on the wing chord. The Delft-Pazy wing model was mounted vertically in the test section on a six-degree-of-freedom force balance, which is attached to a rotating table that allows to set the geometric angle of attack, α, with respect to the steady inflow. The balance and the rotating table are located underneath a splitter plate to reduce wind tunnel interference effects. The wind tunnel setup with an indication of the relevant components is shown in Figure 3.

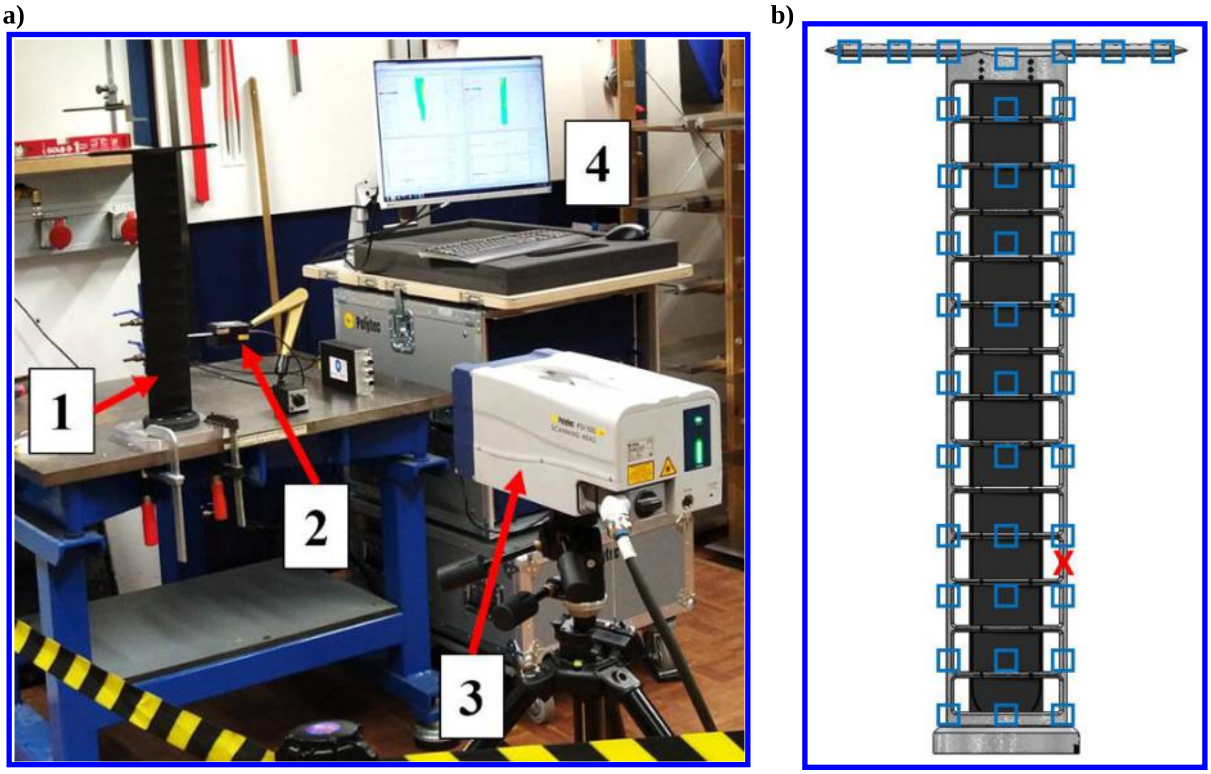

Figure 2: a) Experimental setup for the ground vibration test. 1: Delft-Pazy wing, 2: modal hammer, 3: laser scanning vibrometer, 4: data acquisition computer, b) CAD model of the wing without skin, with an indication of the GVT measurement points (blue squares) and the driving point (red cross)

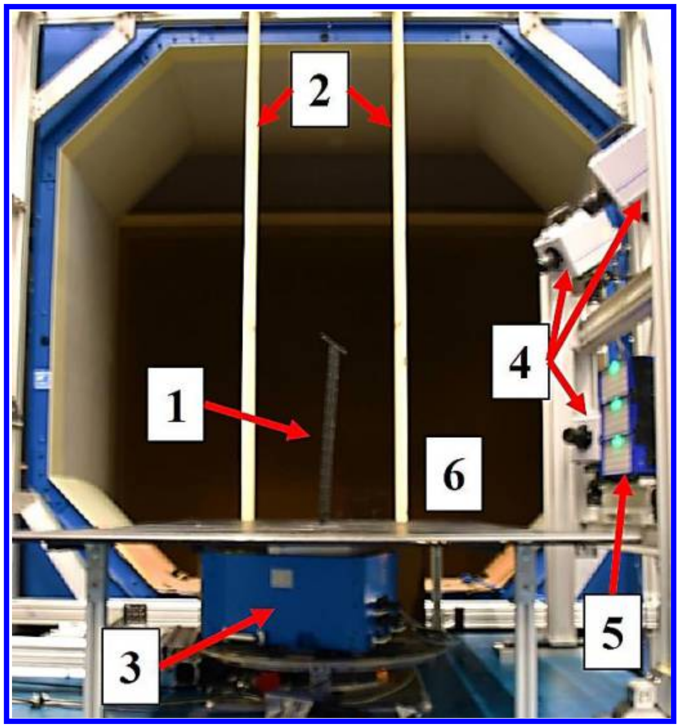

Figure 3: Photo of the wind tunnel setup in the OJF, looking upstream. 1: Delft-Pazy wing, 2: gust generator vanes, 3: six-component balance, 4: 3x high speed cameras, 5: 3x LED illumination units, 6: HFSB seeding generator, placed in the wind tunnel settling chamber (not visible in the photo)

For the experiment, a gust generator is mounted at the wind tunnel nozzle exit, which consists of two vertically mounted gust vanes that span the height of the wind tunnel nozzle [20]. Three different test cases are considered for this study, which correspond to different levels of wing deformation and steady as well as unsteady periodic inflow conditions. The unsteady inflow is generated by a continuous sinusoidal operation of the gust generator during the measurement, with the gust vane angle described by $\beta = \beta_g \cos(2\pi f_g t)$, where β_g and f_g are the amplitude and frequency of the gust vane motion, respectively. The test conditions of the three test cases in this study are summarized in Table 1. The maximum wingtip deflection d_{max} (measured at the center of the wingtip rod) is indicated for each test case as percentage of the span s.

Table 1: Summary of conditions in different test cases

Test case no.	Geometric angle of attack α	Gust actuation frequency f_g	Reduced frequency $k = f_g \pi c / U_\infty$	Gust actuation amplitude β_g	Maximum wingtip deflection d_{max}/s
Case 1	5°	N/A	$k = 0$	0°	8.5 %
Case 2	10°	N/A	$k = 0$	0°	15.9 %
Case 3	10°	3.2 Hz	$k = 0.05$	5°	24.3%

For conducting the LPT measurements of the flow, the freestream is seeded with helium-filled soap bubbles (HFSB) with a diameter of about 0.5 mm that are used as flow tracers. The HFSB seeding generator, which consists of 200 bubble-generating nozzles over an area of approximately 0.5 m in width and 1 m in height, is placed in the settling chamber of the OJF upstream of the wind tunnel nozzle, to minimize the influence of the seeding generator on the freestream and to improve the seeding particle concentration in the test section. The working principle of the nozzles is described in [21]. The seeding particle concentration during the experiment was on the order of 1 cm^{-3}.

The optical measurement setup consists of three Photron Fastcam SA1.1 high speed cameras that are operated at a frequency of 5.4 kHz with a resolution of 1 megapixel (12-bit, 20 µm pixel pitch). The illumination of the HFSB flow tracers and the fiducial markers on the wing is achieved with three LaVision LED-Flashlight 300 illumination units. The size of the measurement volume that was obtained with this setup is about $300\,\text{mm} \times 300\,\text{mm} \times 300\,\text{mm}$. The LPT data acquisition is performed with the LaVision Davis 10 software.

To achieve the complete aeroelastic characterization of the Delft-Pazy wing in the wind tunnel, measurements of the flow field around the entire wing are necessary. Considering the measurement volume size and the limited optical access of the measurement setup, four separate measurements are performed for each test case to achieve this, each covering one part of the entire investigated domain: one measurement on the suction and one on the pressure side for the upper and the lower half of the wingspan, respectively. The four different measurements are then combined into a single time-averaged (for cases 1 and 2) or phase-averaged (case 3) representation during the LPT data processing, that is described in the following section. This averaging is also beneficial to improve the measurement resolution, considering the limited HFSB particle concentration. The adjustment of the spanwise position of the measurement volume is performed by changing the position of the cameras and illumination with respect to the wing. In contrast, the LPT measurements on the suction and pressure side of the wing are performed without moving the optical measurement setup and instead by changing the angle of attack from a positive value of α to the corresponding negative value $-\alpha$, thereby exploiting the symmetry of the Delft-Pazy wing.

D. Lagrangian Particle Tracking Data Processing

The processing of the acquired LPT data is performed with the LaVision Davis 10 software and begins with the geometrical calibration of the measurement system and a volume self-calibration [22]. Successively, the flow tracers are separated from the structural markers in the acquired images, so that a non-uniform optical transfer function [23] can be generated for the structural markers and the flow tracers separately. The removal of the structural information from the integrated measurement images is achieved with a temporal high-pass filter [24], exploiting the different time scales between the flow and the structural motion. The reverse operation is applied to obtain the image data of the structural markers without the flow tracer information, by using a temporal low-pass filter [25]. The image separation procedure is illustrated in Figure 4.

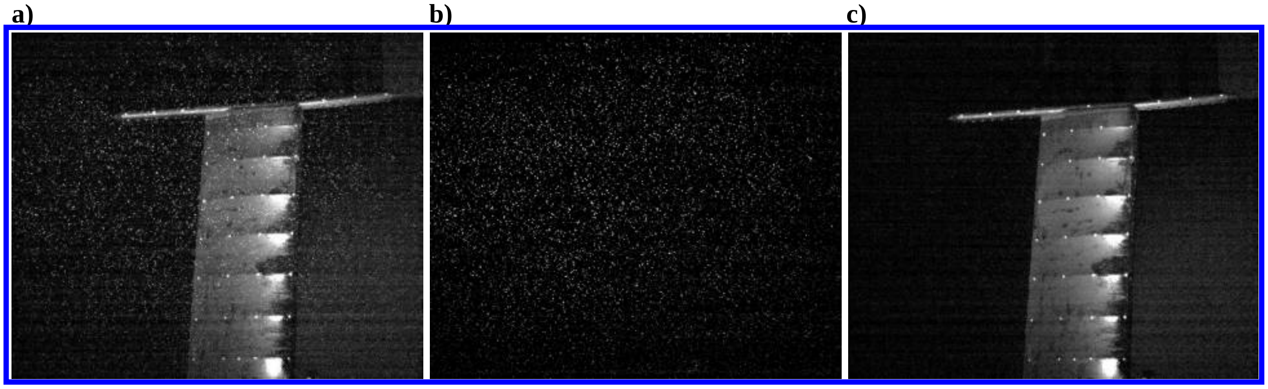

Figure 4: Image processing, a) Combined flow and structure, b) isolated flow tracers, c) isolated structure

After separating the flow and structural information and completing the optical calibration, the next step is to perform the LPT analysis, for which the Shake-The-Box algorithm is used in this study [16]. The results are obtained in terms of individual Lagrangian particle tracks, with position, velocity and acceleration of each particle over time, for both the structural markers and the flow tracers in separate data sets. For the steady inflow measurements, the particle tracks from all acquired images are collected in one data set. For the measurements with dynamic periodic inflow, the particle tracks are postprocessed in a phase-averaged sense based on the recorded signal of the gust generator motion. The particle tracks are assembled in 100 temporal bins, each spanning 1% of the gust excitation period. The further post-processing of the particle tracks to evaluate the quantities of interest for this study are described in Sections IV.B and V.

A further necessary post-processing step of the LPT data is the transformation of the measurement coordinate system to the wind tunnel coordinates. This is achieved by acquiring a reference measurement of the structural markers on the wing without wind tunnel operation after each modification of the measurement volume. This data is then correlated with the reference positions of the markers painted on the model to determine the translations and rotations of the measurement coordinates with respect to the wind tunnel coordinates, which are then used to transform the LPT measurements into the wind tunnel coordinate system.

IV. Structural Characterization

A. Correlation Between FEM Model and GVT Results

A comparison between the experimental results from the GVT and the modal analysis of the FEM model is performed using the SimCenter 3D software. The results are shown in Figure 5 and in Table 2. Figure 5 shows a qualitative comparison between the first five modes. The agreement between the mode shapes is very good which is also indicated by very high values of the modal assurance criterion (MAC, [26]) shown in Table 2.

Table 2: Comparison of the first five eigenfrequencies between the FEM model and GVT results and modal assurance criterion for the Delft-Pazy wing, with and without skin

Mode no.	Mode type	Without skin				With Oralight skin			
		f_{FEM}	f_{GVT}	Δf	MAC	f_{FEM}	f_{GVT}	Δf	MAC
1	First bending	2.8 Hz	2.9 Hz	-1.3%	0.92	3.3 Hz	3.2 Hz	+2.3%	0.96
2	Second bending	18.9 Hz	19.7 Hz	-3.9%	0.98	21.9 Hz	22.5 Hz	-2.3%	0.99
3	First torsion	24.9 Hz	25.0 Hz	-0.7%	0.97	28.1 Hz	29.5 Hz	-4.7%	0.97
4	Third bending	54.7 Hz	57.2 Hz	-4.4%	0.97	63.1 Hz	65.0 Hz	-2.9%	0.96
5	Second torsion	94.4 Hz	103.5 Hz	-8.8%	0.82	105.9 Hz	119.7 Hz	-11.5%	0.73

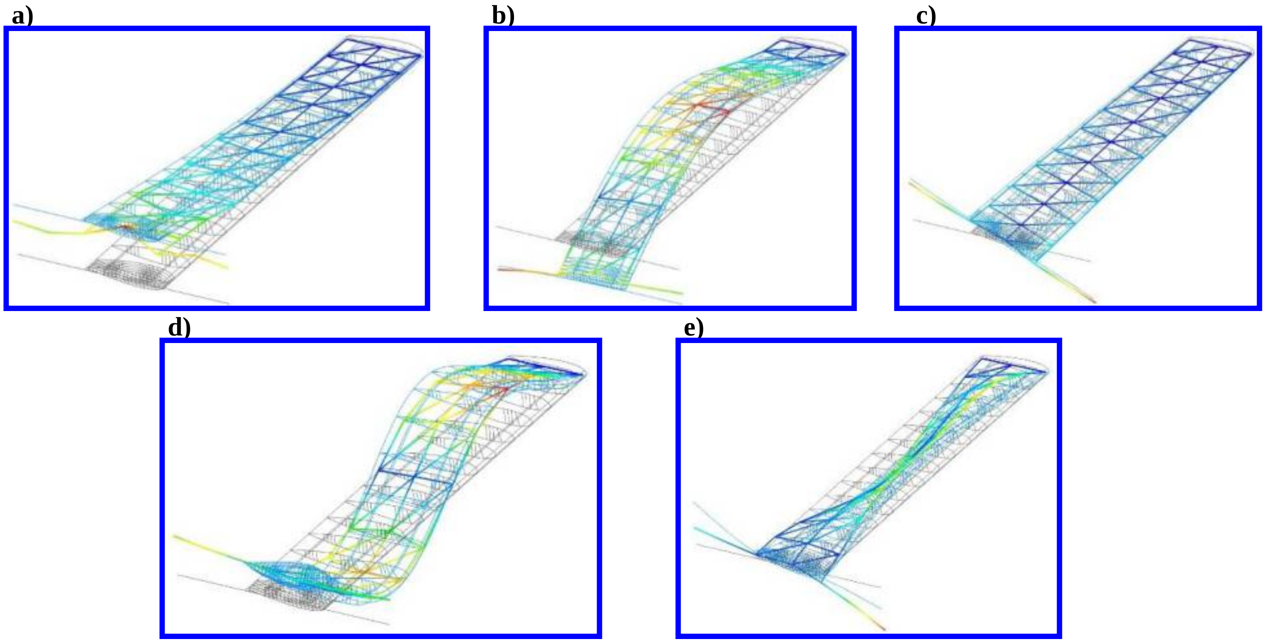

Figure 5: Dynamic mode shape comparison between FEM model (light blue, with undeformed reference shape in grey) and GVT result (colored by displacement). a) first bending, b) second bending, c) first torsion, d) third bending, e) second torsion

Table 2 also shows the effect of using the Oralight foil as the wing skin on the modal frequencies, by including the FEM and GVT results for the model with and without the skin. The Oralight skin has a significant effect on the stiffness of the wing, which increases the modal frequencies consistently by about 10%. The agreement between the frequencies of the FEM model, f_{FEM}, and from the GVT, f_{GVT}, for the first five modes is very good, with an average difference of around 4% of the FEM model with respect to the GVT result, $\Delta f = (f_{FEM} - f_{GVT})/f_{GVT}$, which is similar to the agreement between the FEM and the GVT results reported in [5]. The level of agreement between the FEM and experimental results in terms of the frequency difference and MAC value is not critically affected by the presence of the skin.

B. Wind Tunnel Measurements

After the LPT measurements of the fiducial markers are transformed to the wind tunnel coordinate system as described in Section III.D, the marker position measurements are used to determine the deformed shape of the entire wing. This is achieved by calculating the chordwise average value of the marker position for each spanwise section where the markers were painted (i.e., the ribs of the wing) and then fitting a polynomial through these measurements along the spanwise direction. Following this procedure, the polynomial curve fit can be used as a reference spanwise axis to calculate the deformed wing shape. A fourth order polynomial is used in this study for the curve fit, which satisfies the geometric boundary conditions of a wing clamped at the root, $d = 0$ and $d'(z = 0) = 0$, and is defined as:

$$d(z) = Az^4 + Bz^3 + Cz^2,$$

where the coefficients A, B and C are optimized to provide the best fit to the experimental measurements in a least-squares sense. The results of the polynomial curve fit to the marker measurements for the static test cases 1 and 2 are shown in Figure 6. The individual marker measurements for these test cases are averaged from 1000 images acquired in the wind tunnel measurement to reduce the effect of measurement noise and small-scale vibrations of the wing during the experiment. The polynomial fit accounts for the large deflections by maintaining the arc length of the curve constant with respect to the undeformed shape, assuming that the arc length does not change due to deformation. This is achieved by numerically integrating the length of the polynomial curve to determine the value of z_{tip} in the deformed case that corresponds to an arc length that is equal the value of z_{tip} in the undeformed case.

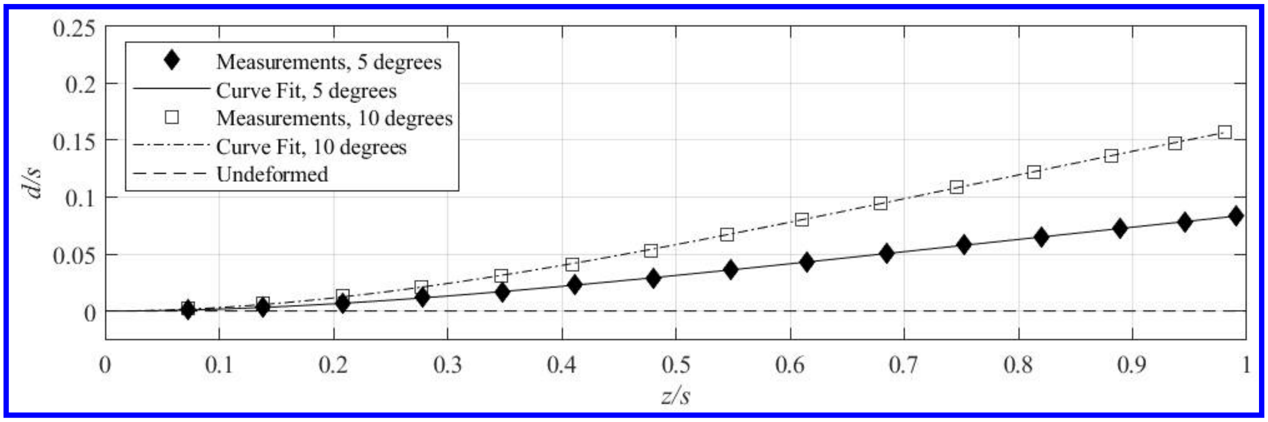

Figure 6: Displacement measurements along the span with polynomial curve fit for the test cases 1 and 2

The standard deviation of the residual between the 15 measurement data points along the span and the curve fit is very small, at $\sigma_1 = 0.13$ mm in test case 1 and $\sigma_2 = 0.25$ mm in test case 2, corresponding to 0.28% and 0.29% of the respective wingtip displacement. To determine the wing shape, the torsional deformation in terms of a twist angle ε of the wing around the reference axis is required as well. The twist angle is estimated from the marker measurements by first calculating the average displacements of the two marker measurements near the leading edge (LE) and near the trailing edge (TE). The experimental twist angle along the span is then given as:

$$\varepsilon(z) = \tan^{-1}\left(\frac{y_{TE}(z) - y_{LE}(z)}{x_{TE}(z) - x_{LE}(z)}\right).$$

The experimentally determined twist angles in both test cases were found to be small with $|\varepsilon| < 0.4°$ across the entire span. To simplify the analysis and avoid the influence of random errors, it is therefore assumed that the wing does not twist. Based on this assumption, the wing shape is reconstructed as shown in Figure 7, where it is shown together with the experimental marker measurements.

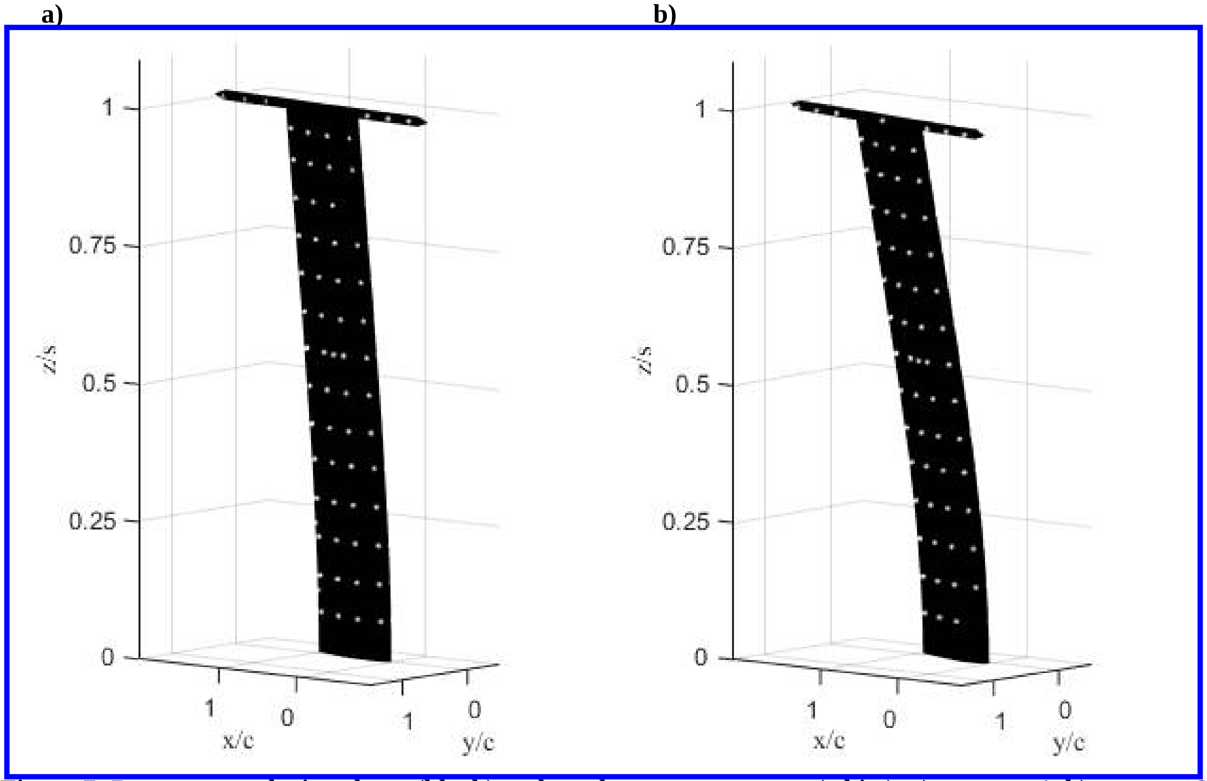

Figure 7: Reconstructed wing shape (black) and marker measurements (white), a) test case 1, b) test case 2

For test case 3 with unsteady periodic inflow, the marker measurements are analyzed in a phase-averaged sense, analogous to the flow measurements, which means that measurements from different periods are collected at the respective time as fraction of the period, t/T. To reduce the effect of measurement noise and outliers, a temporal smoothing procedure using a sinusoidal curve fit is applied, as illustrated in Figure 8. Because of the large deformations, the temporal behavior of the wing deflection is not expected to be an ideal sinusoid in the refence coordinate system of the undeformed wing. The temporal smoothing is therefore performed after transforming the marker measurements into the reference system of the static deflected wing shape of case 2. In this reference system, the measurements of the marker position are obtained in terms of displacements normal to the static deflected position, as shown in Figure 8. With this approach, the sinusoidal curve fit provides a very good approximation of the temporal behavior, with a standard deviation of the residual of the fit on the order of $\sigma_{\text{sin}} \approx 0.2$ mm. After the phase-averaged marker measurements are determined, the same curve fitting procedure as for test cases 1 and 2 can be applied per phase instant to the data from test case 3 to yield the phase-averaged behavior of the wing deformation, as shown in Figure 9 for the phase instants with the minimum and maximum deflection.

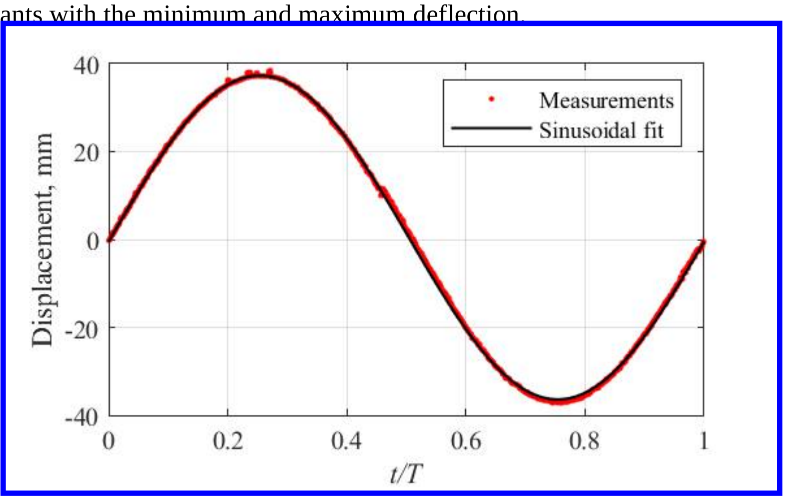

Figure 8: Measurements of deflection over the period for the marker at z/s=0.9 with sinusoidal curve fit

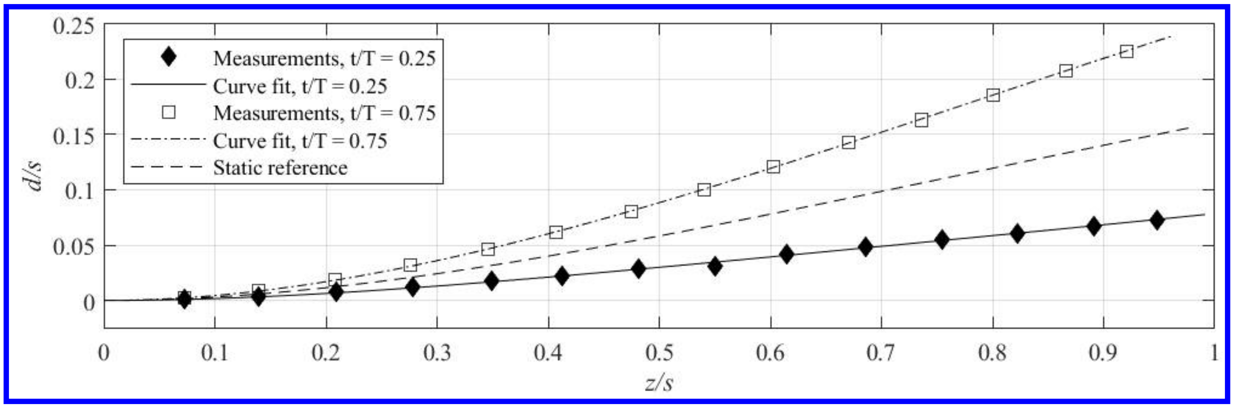

Figure 9: Polynomial curve fit for test case 3 at different phase instants

V. Aerodynamic Characterization

To characterize the static aerodynamic behavior of the Delft-Pazy wing, the lift coefficient as measured with the six-component balance for the angle of attack range $-15° < \alpha < +15°$ is shown in Figure 10. This corresponds to the range of effective inflow angles for the three test cases in Table 1. The lift slope $\partial C_L/\partial\alpha$ is nearly constant in the interval between $-8° < \alpha < +8°$, as expected from linear aerodynamics theory. The lift slope then declines until $C_{L,max}$ is reached at around $\alpha = 12°$, after which the wing is in stall.

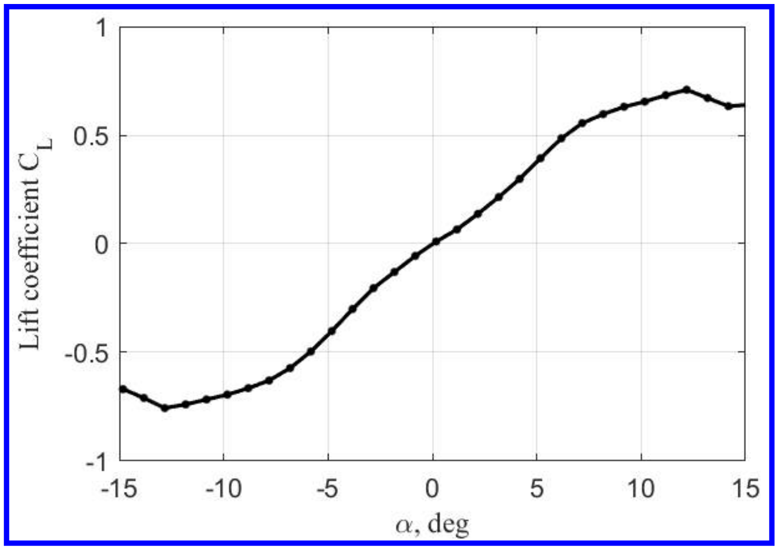

Figure 10: Balance measurements of the lift coefficient for different of angles of attack

The LPT data in the wind tunnel reference frame, that is obtained after combining the data from different acquisitions that is described in Section III.D, is shown for the cases test 1 and 2 in Figure 11.a) and Figure 11.b), respectively, as well as for test case 3 in Figure 12. The depicted LPT data corresponds to a spanwise section of the flow field within 1% of the span around the spanwise stations $z/s = 0.6$ (test cases 1 and 2) and $z/s = 0.4$ (test case 3) and is colored by streamwise velocity. The position of the wing section that is shown in the plots is based on the wing shape reconstruction described in Section IV.B.

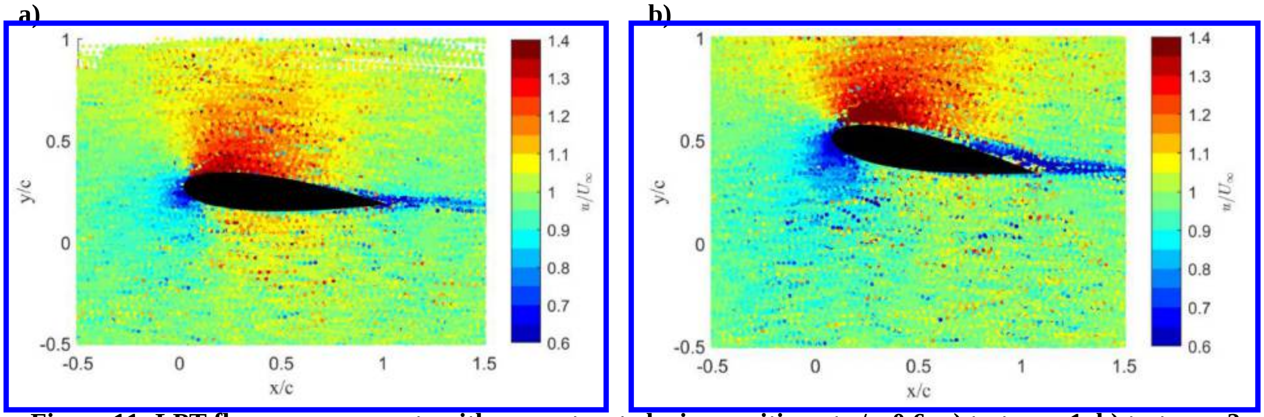

Figure 11: LPT flow measurements with reconstructed wing position at z/s=0.6, a) test case 1, b) test case 2

Despite the presence of random measurement errors, the main features of the flow field, such as the stagnation point near the leading edge on the pressure side, the flow acceleration over the suction side, as well as the thin wake, are clearly captured in the LPT data. For test cases 2 and 3, a region of separated flow can be identified near the trailing edge on the suction side. This onset of trailing edge stall at $\alpha = 10°$ is in good agreement with the decrease in lift slope that was observed for $|\alpha| > 8°$ in Figure 10. The extent of this phenomenon in test case 3 depends on the effective angle of inflow, as visible in Figure 12.a), where the phase instant $\mathrm{t/T} = 0$ corresponds to the wing moving in the positive y-direction, hence reducing the effective inflow angle and thus limiting the extent of trailing edge stall. The opposite effect is visible in Figure 12.c) at $\mathrm{t/T} = 0.5$, where the motion of the wing increases the effective inflow angle and the region of separated flow near the trailing edge is therefore enlarged. In the cases of $\mathrm{t/T} = 0.25$ and $\mathrm{t/T} = 0.75$, shown in Figure 12.b) and d) respectively, the wing's velocity is zero and the extent of the trailing edge separation is hence similar to the static situation shown in Figure 11.b).

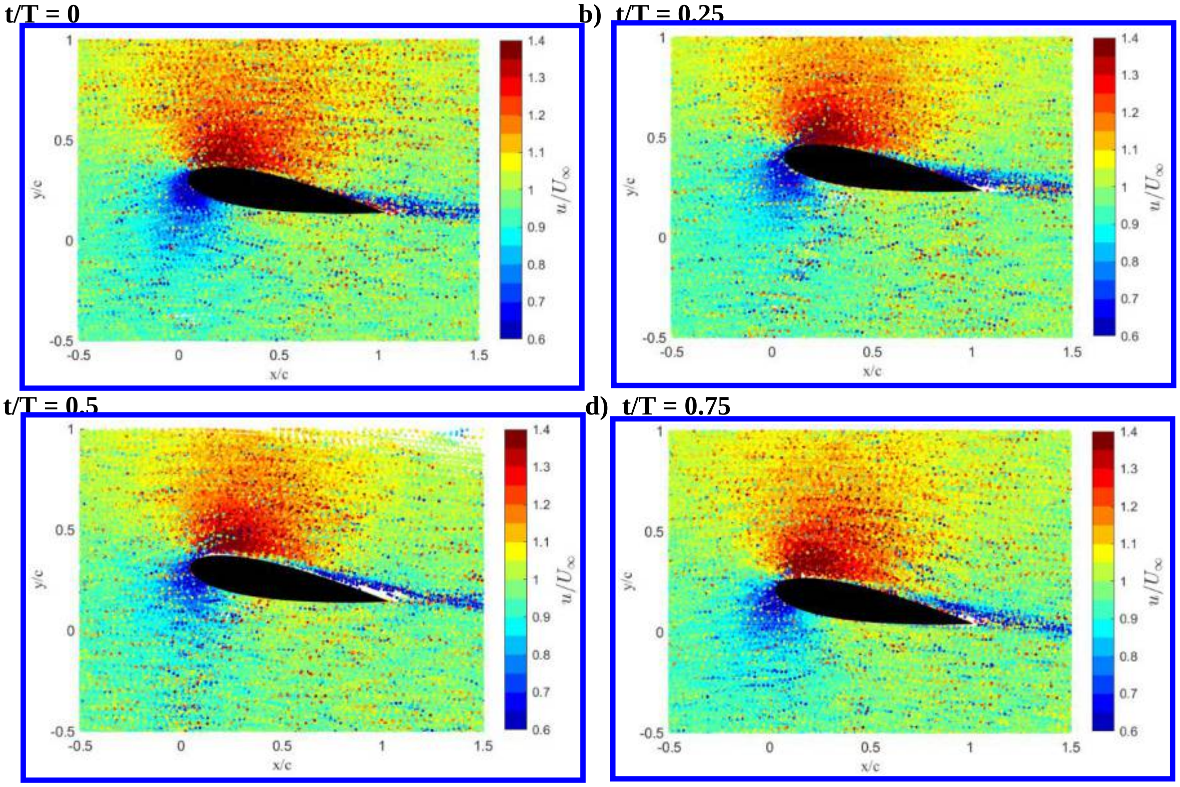

a) t/T = 0

b) t/T = 0.25

c) t/T = 0.5

d) t/T = 0.75

Figure 12: Phase averaged LPT flow measurements with reconstructed wing position at z/s=0.4 for test case 3

A convenient way to retrieve the lift force from the measured velocity fields is through the circulation around the wing. The Kutta-Joukowski theorem relates the sectional lift force L' to the circulation Γ [27]:

$$L' = \rho U_\infty \Gamma,$$

where the circulation is defined as the line integral of the flow velocity over a path C enclosing the wing section

$$\Gamma = -\oint_C \vec{u} \cdot d\vec{s}.$$

Although the Kutta-Joukowski theorem is derived on the assumption of steady potential flow, previous studies have shown that it can be used to determine the lift accurately from experimental data for situations that exhibit moderate effects of viscosity [17], when the circulation is calculated from velocity measurements outside of the region affected by these viscous effects. In this study, the circulation is determined from the LPT measurements with a gridless approach [28] by defining an elliptic path around the particular wing section of interest and integrating the velocity data within a prescribed distance r around this path.

The lift force acts perpendicular to the freestream and the spanwise axis of the wing. Therefore, the elliptic integration paths are defined in a local coordinate system of the respective wing section of interest, which has its origin at the mid-chord position of the wing section. The circulation determination procedure is visualized for test case 2 for 20 wing sections along the span in Figure 13.a), where the LPT data is shown as a collection of data along such an elliptical path. The velocity tangential to the elliptic path for the LPT data at spanwise location $z/s = 0.6$ is shown in Figure 13.b). The filtered tangential velocity is determined from the LPT track data with a smoothing spline and is integrated along the path to obtain the circulation. The results for the distribution of the lift along the span for the test cases 1 and 2 are shown in Figure 14. A comparison between the LPT-based lift force integrated along the span and the measurements of the root force perpendicular to the inflow is shown in Table 1, where the differences are small at around 2%. A more detailed discussion of the performance of the gridless loads determination for the test cases 1 and 2 can be found in [28].

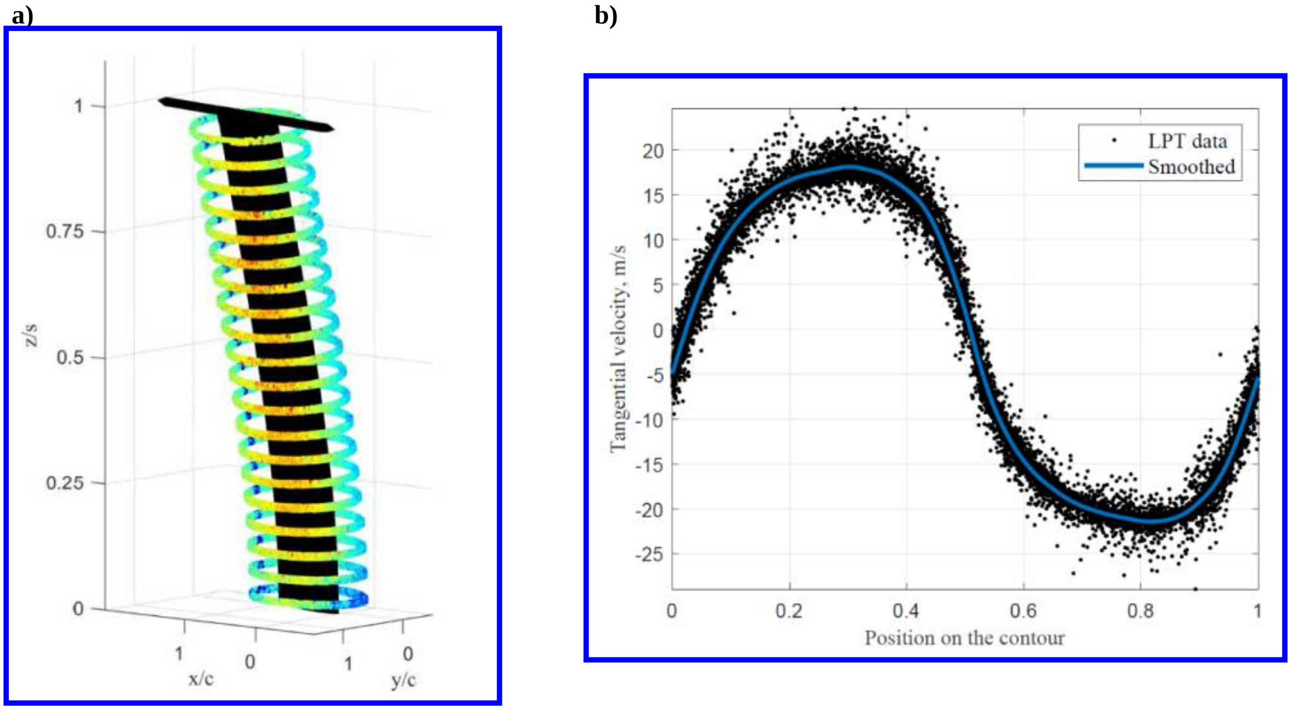

Figure 13: Test case 2, a) LPT data along elliptical paths, b) tangential velocity along the path at z/s=0.6

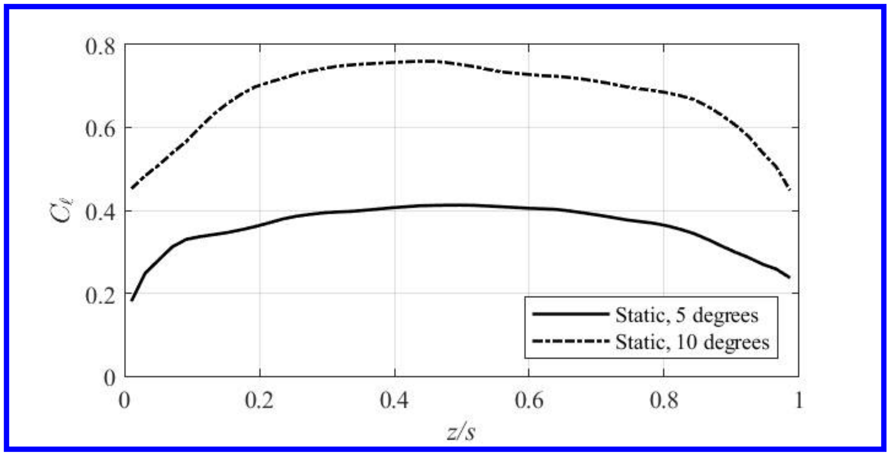

Figure 14: Lift along the span as determined by measurements of the circulation for test cases 1 and 2

Table 3: Comparison of the LPT-based lift with the balance measurements for test cases 1 and 2

Test case no.	Lift force L		
	LPT based	Balance	Difference LPT/Balance
Case 1	4.03 N	4.12 N	-2.08%
Case 2	7.49 N	7.64 N	-1.96%

In unsteady inflow conditions, the flow acceleration effects, which are not captured by measuring only the circulation, have an influence on the lift force as well. However, for the relatively low reduced frequency in this study of $k = 0.05$ for test case 3, the flow may be considered as quasi-steady [29], which justifies the use of the Kutta-Joukowsky theorem for the determination of the lift force for this case as well. The dynamic behavior of the lift in test case 3 is shown in Figure 15. Overall, the lift distributions at different phase instants in Figure 15.a) are similar to the static reference lift distribution for the same geometric angle of attack from case 2. However, the variation of the lift along the span differs for different phase instants. For example, the lift distribution at the phase instant $t/T = 0.5$ shows a decrease in lift near the root and a small lift increase towards the tip, when compared to the static reference lift, whereas the lift distribution at $t/T = 0$ has the opposite trend, while both of these phase instants correspond to a similar deformed wing shape as the static reference. In Figure 15.b), the temporal behavior of the lift variation from the mean is shown for different spanwise locations. The variation of the lift near the root is similar to a cosine signal, as expected from the gust generator excitation. Further outboard, the structural motion of the wing affects the aerodynamics. As a result, the lift variation decreases, while near the tip at $z/s = 0.8$, the variation of the lift does not correspond to a cosine shape anymore.

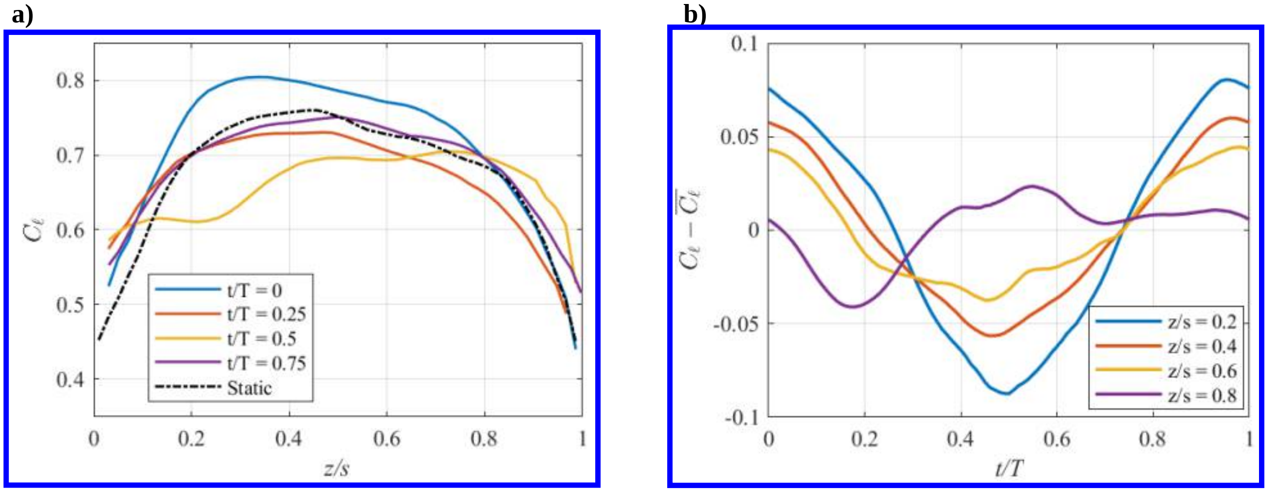

Figure 15: Unsteady lift in test case 3, a) lift along the span at four phase instants with static reference, b) lift over the period at four spanwise locations

The temporal behavior of lift integrated along the span for test case 3 is shown in Figure 16. The qualitative behavior of the wing deflection is indicated for reference. As expected, the mean value of the dynamic lift is with a +1.3% difference not considerably changed with respect to the static reference lift. The variation of the lift over the period has a relatively small peak-to-peak amplitude of 0.06 lift coefficient counts. The relatively large deflection response of the wing to this excitation can be explained from the proximity of the gust excitation frequency to the frequency of the first bending mode of the wing. This proximity also produces the phase difference between excitation force (i.e., lift) and structural response (i.e., out of plane deflection) that is observed in Figure 16. The observed lag between lift variation and wing motion is approximately $\Delta\, t/T = 0.28$, which is close to the phase lag of 90° occurring when the excitation frequency is at the eigenfrequency of a harmonically forced system [30], such that the lift force is in phase with the wing's velocity and hence does positive work on the structure.

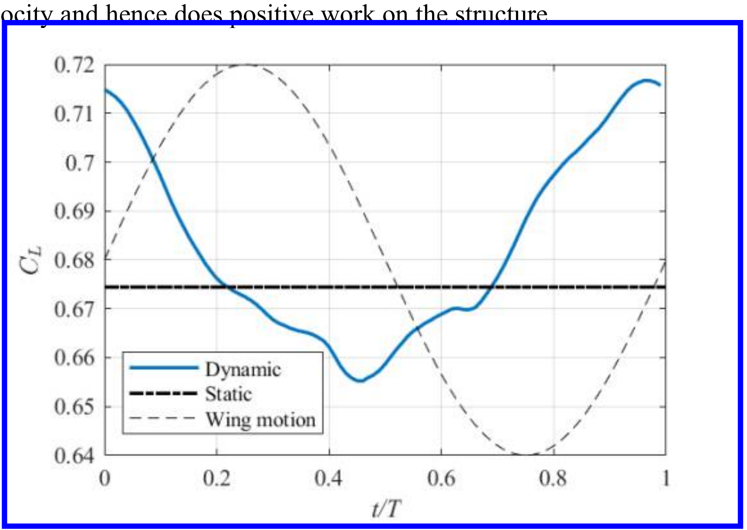

Figure 16: Lift on the wing integrated over then span for test case 3

VI. Aeroelastic Validation

The experimental data acquired in the aerodynamic and structural measurements can be used to perform an aeroelastic validation of numerical aeroelastic prediction models. All aeroelastic models consist of two separate models, an aerodynamic and a structural model. The principle of an aeroelastic validation using the experimental data of this study is to first compare the aerodynamic loads that are produced with an aerodynamic model to the experimental results, obtained by the measurements of the circulation, to assess the quality of this numerical prediction. Afterwards, the quality of the structural model can be assessed by applying the experimentally determined loads to the structural model and then comparing the structural response to the experimental measurements of the wing shape. This step is demonstrated in Figure 17, where the structural response of the linear static FEM model to the experimentally determined aerodynamic loads for the static test cases is compared to the measurements of the deformed wing shape. The simulation results of the linear FEM model under predict the experimental deflection measurements. The tip displacement is clearly underestimated in both test cases, by -16.7% of the respective experimental tip displacements. Furthermore, it can be observed that the linear model does not capture the span shortening effect that occurs due to the large deformations, which not only affects the deflection, but also causes a small mismatch in the spanwise location of the sampling points between model and experiment.

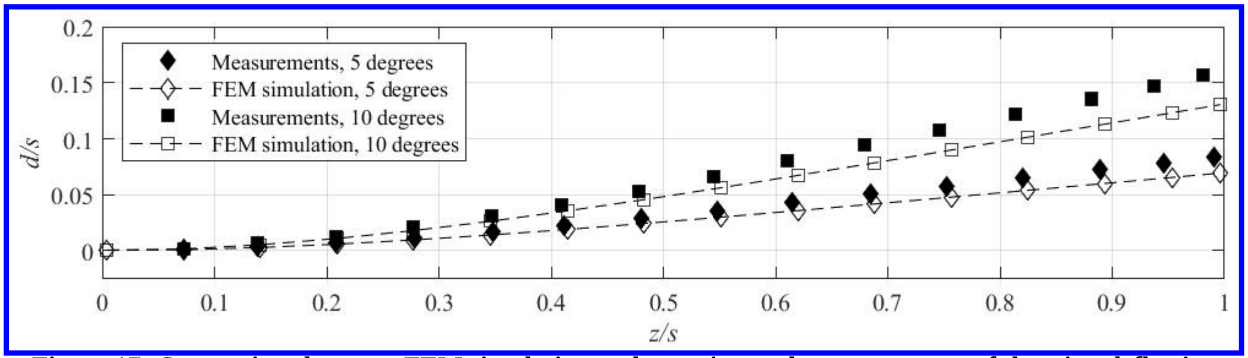

Figure 17: Comparison between FEM simulation and experimental measurements of the wing deflection

VII. Conclusion and Outlook

This study has demonstrated an experimental approach that allows for the aeroelastic characterization of flexible wings in wind tunnel tests. The experimental approach was applied to two different steady and one unsteady flow situation. It consists of integrated aerodynamic and structural measurements that are conducted with a single optical measurement system. In this approach, aerodynamic loads are determined from measurements of the flow velocity and the integral force results are found to be in good agreement with reference data from a force balance. The measurements of structural marker positions were used to reconstruct the deflected shape of the wing under aerodynamic load. The negligible differences between the measurements and the smooth shape reconstructions indicate the suitability of this shape measurement approach to test cases with very large deformations.

The experimental characterization data from the wind tunnel can be used to perform an aeroelastic validation of numerical models, as demonstrated in this study for a linear FEM model, which was found to be a good representation of the experimental wing by comparing numerical modal analysis results with experimental modes obtained from a GVT. It was demonstrated that the linear FEM model does not perform accurately for the large deformations that the wing is subjected to in this study, and a more sophisticated model will be necessary to produce accurate numerical aeroelastic predictions.

Future activities related to the present study are the comparison of the experimental results with nonlinear aeroelastic models that are better suited to model the behavior of such highly flexible wings. Furthermore, the validation activities can be extended to the experimental test case with unsteady periodic inflow.

VIII. Data Archive

The experimental data that is presented in this article will be made available in a data archive of the 4TU.ResearchData center that can be found under the DOI: https://doi.org/10.4121/c.5720456

IX. Acknowledgements

The authors appreciate the contribution of Ariel Drachinsky and Daniella E. Raveh to this work by providing the geometry and the FEM model of the Pazy wing and by offering advice for the construction of the Delft-Pazy wing. Furthermore, the authors gratefully acknowledge the help of José L. Costa Fernández and Adrián Grille Guerra during the wind tunnel experiment and with the LPT data processing. This work has been carried out in the context of the HOMER (Holistic Optical Metrology for Aero-Elastic Research) project that has received funding from the European Union's Horizon 2020 research and innovation programme under grant agreement No 769237.

X. References

1. Dimitriadis, G., *Introduction to Nonlinear Aeroelasticity*, First Edition, John Wiley & Sons Ltd., 2017.
2. Bernhammer, L. O., de Breuker, R., and Karpel, M., "Geometrically Nonlinear Structural Modal Analysis Using Fictitious Masses," *AIAA Journal*, Vol. 55, No. 10, 2017.
3. Kantor, E., Raveh, D. E., and Cavallaro, R., "Nonlinear-Structural-Nonlinear-Aerodynamic Model for Static Aeroelastic Problems," *AIAA Journal*, Vol. 57, No. 5, 2019.
4. Drachinsky, A., and Raveh, D. E., "Modal Rotations: A Modal-based Method for Large Structural Deformations," *AIAA Journal*, 2020.
5. Avin, O., Raveh, D. E., Drachinsky, A., Ben-Shmuel, Y., and Tur, M., "An Experimental Benchmark of a Very Flexible Wing," *AIAA SciTech Forum*, 2021.
6. Collar, A. R., "The Expanding Domain of Aeroelasticity," *The Aeronautical Journal*, Vol. 50, No. 428, 1946.
7. Tang, D., and Dowell, E., "Experimental Aeroelastic Models Design and Wind Tunnel Testing for Correlation with New Theory," *Aerospace*, Vol. 3, No. 2, 2016.
8. Liu, T., Burner, A. W., Jones, T. W., and Barraows, D. A., "Photogrammetric techniques for aerospace applications," *Progress in Aerospace Sciences*, Vol. 54, pp. 1-58, 2012.
9. Raffel, M., Willert, C. E., Scarano, F., Kähler, C. J., Wereley, S., and Kompenhans, J., *Particle Image Velocimetry: A Practical Guide*, 3rd ed., Springer, 2018.
10. Gherlone, M., Cerracchio, P., and Mattone, M., "Shape sensing methods: Review and experimental comparison on a wing-shaped plate," *Progress in Aerospace Sciences*, Vol. 99, pp. 14–26, 2018.
11. van Oudheusden, B. W., "PIV-based pressure measurement," *Measurement Science and Technology*, Vol. 24, No. 3, 2013.
12. Rival, D. E., and van Oudheusden, B. W., "Load-estimation techniques for unsteady incompressible flows," *Experiments in Fluids*, Vol. 58, No. 3, 2017.
13. Liu, T., Montefort, J., Gregory, J., Palluconi, S., Crafton, J., and Fonov, S., "Wing Deformation Measurements from Pressure Sensitive Paint Images Using Videogrammetry," *41st AIAA Fluid Dynamics Conference and Exhibit*, 2011.
14. Marimon Giovannetti, L., Banks, J., Turnock, S. R., and Boyd, S. W., "Uncertainty assessment of coupled Digital Image Correlation and Particle Image Velocimetry for fluid-structure interaction wind tunnel experiments," *Journal of Fluids and Structures*, Vol. 68, 2017.
15. Zhang, P., Peterson, S. D., and Porfiri, M., "Combined particle image velocimetry/digital image correlation for load estimation," *Experimental Thermal and Fluid Science*, Vol. 100, 2019.
16. Schanz, D., Gesemann, S., and Schröder, A., "Shake-The-Box: Lagrangian particle tracking at high particle image densities," *Experiments in Fluids*, Vol. 57, No. 5, 2016.
17. Mertens, C., Sciacchitano, A., van Oudheusden, B. W., and Sodja, J., "An integrated measurement approach for the determination of the aerodynamic loads and structural motion for unsteady airfoils," *Journal of Fluids and Structures*, Vol. 103, 2021.
18. Scarano, F., Ghaemi, S., Caridi, G. C. A., Bosbach, J., Dierksheide, U., and Sciacchitano, A., "On the use of helium-filled soap bubbles for large-scale tomographic PIV in wind tunnel experiments," *Experiments in Fluids*, Vol. 56, No. 2, 2015.
19. Mertens, C., de Rojas Cordero, T., Sodja, J., Sciacchitano, A., and van Oudheusden, B. W., "Aeroelastic Characterization of a Flexible Wing Using Particle Tracking Velocimetry Measurements", *AIAA Journal*, 2021.
20. Lancelot, P. M. G. J., Sodja, J., Werter, N. P. M., and de Breuker, R., "Design and testing of a low subsonic wind tunnel gust generator," *Advances in Aircraft and Spacecraft Science*, 4(2), pp. 125-144, 2017.
21. Faleiros, D. E., Tuinstra, M., Sciacchitano, A., Scarano, F., "Generation and control of helium-filled soap bubbles for PIV," *Experiments in Fluids*, 60(40), 2019.
22. Wieneke, B., "Volume self-calibration for 3D particle image velocimetry," *Experiments in Fluids*, Vol. 45, No. 4, 2008.

23. Schanz, D., Gesemann, S., Schröder, A., Wieneke, B., and Novara, M., "Non-uniform optical transfer functions in particle imaging: calibration and application to tomographic reconstruction," *Measurement Science and Technology*, Vol. 24, No. 2, 2013.
24. Sciacchitano, A., and Scarano, F., "Elimination of PIV light reflections via a temporal high pass filter," *Measurement Science and Technology*, Vol. 25, No. 8, 2014.
25. Mitrotta, F. M. A., Sciacchitano, A., Sodja, J., de Breuker, R., and van Oudheusden, B. W., "Experimental investigation of the fluid-structure interaction between a flexible plate and a periodic gust by means of Robotic Volumetric PIV," 13th International Symposium on Particle Image Velocimetry, edited by C. J. Kähler, R. Hain, S. Scharnowski, and T. Fuchs, 2019.
26. Pastor, M., Binda, M., and Harčarik, T., "Modal assurance criterion", *Procedia Engineering*, Vol. 48, p. 543-548, 2012.
27. Anderson, J. D., Jr., *Fundamentals of Aerodynamics*, 6th Edition, McGraw-Hill Education, 2017.
28. Mertens, C., Costa Fernández, J. L., Sciacchitano, A., van Oudheusden, B. W., and Sodja, J., "Gridless Determination of Aerodynamic Loads Using Lagrangian Particle Tracks", *14th International Symposium on Particle Image Velocimetry*, 2021.
29. Leishman, J. G., *Principles of Helicopter Aerodynamics*, 2nd Edition, Cambridge University Press, 2016.
30. Weaver Jr, W., Timoshenko, S.P. and Young, D.H, *Vibration problems in engineering*, 5th Edition, John Wiley & Sons, 1991.